Inversion of deformation fields time-series from optical images, and application to the long term kinematics of slow-moving landslides in Peru

Noélie Bontemps[*], Pascal Lacroix, Marie-Pierre Doin

Univ. Grenoble Alpes, CNRS, IRD, IFSTTAR, ISTerre, 38000 Grenoble, France

ABSTRACT

Slow-moving landslides are numerous in mountainous areas and pose a large threat to populations. Many observations show that their kinematics is driven by climatic forcings and earthquakes. In this study, we document the complex interaction between those two forcings on the slow-moving landslide kinematics, based on the retrieval of landslide displacements over 28-years using optical satellite images. To overcome the decorrelation effect over this large time-span, and possible misalignment between images, we develop a method that uses the redundancy of displacement fields from image pairs to derive a robust time-series of displacement. The method is tested on the 28-year long SPOT1/5-Pléiades archive, over an area in Peru affected by both earthquakes and rainfall. Errors are estimated on stable areas and by comparison with one 13-year long and eleven 3-year long GPS time-series on the Maca landslide. The methodology diminishes by up to 30% the uncertainty and reduces significantly the gaps due to decorrelation. The data set allows detecting 3 major landslides, moving at a rate of 35 to 50 m over 28 years, and smaller landslides with lower displacement rates. Time-series obtained over the three main landslides provide interesting results of their long-term kinematics, primarily driven by precipitation. We propose simple statistical hydro-kinematic models, relating yearly motion to seasonal rainfall, to explain the observed time-series. We found that annual precipitation is controlling the landslide displacements after a certain rainfall threshold is reached. Besides this control, we show the possible impact of a local Mw 5.4 earthquake in 1991 on the kinematics of the Maca landslide. Our results suggest that the earthquake accelerated the landslide and has an effect during several years on the precipitation threshold required for triggering a motion. These results suggest that the rainfall threshold can vary in time following strong earthquakes shaking.

1. Introduction

Slow-moving landslides are mass-movements with velocities ranging from a few centimeters to a few meters per year (Hungr et al., 2014). They can affect human settlements, such as villages and roads, and their economic impact is difficult to estimate because of their long-term time evolution (from a month to several decades, Strozzi et al., 2010). Furthermore, those slow-moving landslides may exhibit sudden acceleration phases and flows that are generally difficult to predict and can result in loss of life (Petley et al., 2002; Jongmans et al., 2009).

The kinematics of those active landslides is found to be primarily driven by precipitation and water infiltration (Iverson, 2000; Zerathe et al., 2016). Other sources of external forcing include river erosion (Eilertsen et al., 2008), earthquakes (Lacroix et al., 2014), glacier retreats (Strozzi et al., 2010), atmospheric tides (Schulz et al., 2009) and human activity (Mansour et al., 2011). All these factors act on different time-scales varying from seconds (earthquakes) to several hundreds or thousands of years (glacier retreat). In countries where both earthquakes and climatic triggering mechanisms are relevant, complex interactions are possible between the two mechanisms, in which one mechanism could enhance the conditions for landslide triggering by fracturing/weakening the medium and/or increasing the pore pressure (Jibson et al., 1994). This process is also corroborated by observations over rapid landslides, where increased rates of landsliding have been observed in the years after large earthquakes (Dadson et al., 2004; Lin et al., 2008; Marc et al., 2015), and proposed to be caused by reversible damage of rock mass. In addition to this damage process, earthquakes have been found to also modify the friction at the base of landslides, accelerating slow-moving landslides over several weeks (Moro et al., 2011; Lacroix et al., 2014) even for medium size earthquakes (Mw 6.0) in dry conditions. The number of observations over slow-moving landslides during earthquakes is however, very limited and the understanding of the complex interaction between rainfall and earthquake forcing still requires more observations. In this context, it is very important to monitor their activity over time.

Remote-sensing techniques based on both radar (e.g. Handwerger

et al., 2013) and optical satellites (e.g. Delacourt et al., 2004) have proven to be efficient for this monitoring purpose. As opposed to Interferometric Synthetic Aperture Radar (InSAR) data, where applications are limited to relatively slow landslides (≤ 1 m/yr) and with favourable slope orientations, optical satellites are particularly well-adapted to monitor objects of small size like landslides, moving at centimeter to decameter rates per year (Kääb, 2002; Casson et al., 2003; Delacourt et al., 2004; Stumpf et al., 2014; Lacroix et al., 2015; Bennett et al., 2016). The landslide motion can be retrieved by a three step process (Leprince et al., 2007) including: (1) orthorectification of the images, (2) coregistration, and(3) correlation between pairs of diachronic images. This process has been applied on pairs of optical images from various platforms, including 0.6 m resolution (pixel-size) Quick-bird images (Delacourt et al., 2004), 0.7 m resolution Pléiades images (Stumpf et al., 2014; Lacroix et al., 2015), 2.5 m resolution SPOT5 images (Leprince et al., 2008), 15 m resolution ASTER images (Kääb, 2002), and 15 m Landsat images (Dehecq et al., 2015). All these studies have shown the possibility to retrieve the ground motion with an accuracy of a fifth of a pixel size (Lacroix et al., 2015).

The monitoring of different objects, as landslides, active faults or glaciers, from optical images is affected by clouds, problems of orthorectification, coregistration errors, shadows, changes of the surface state with time, and vegetation changes with time. All these effects induce noise and outliers in the images. Different post-processing filters have therefore been applied to remove these effects (Berthier et al., 2005; Scherler et al., 2008; Heid and Kääb, 2012; Stumpf et al., 2014, 2017), adapted to each of these problems. Other options to detect and monitor ground deformations have been developed, based on the processing of the full Landsat archive (Dehecq et al., 2015; Fahnestock et al., 2015). Those different studies used the pairwise processing of Landsat to produce time-series of deformation fields. This strategy led to better coverage and lower uncertainties of the deformation fields.

The launch of new constellations of optical satellites, with a very good revisit time (Sentinel-2, 5 days; Landsat-7/8, 8 days at the Equator) increases considerably the number of data available over an area. This revisit time enables the creation of time-series of deformation, of large interest for detecting transient signals over different objects, that can be precursors of catastrophic events. At the same time, these large data sets can be used to reduce the uncertainty of the deformation field. Indeed the pairwise process can be improved by taking into account a large number of possible image pairs, providing redundant measurements. This idea is commonly used by the InSAR community, where interferograms are often performed between optimal pairs of images, with limited perpendicular and temporal baselines. This led to different tools (Berardino et al., 2002; Cavalié et al., 2007; López-Quiroz et al., 2009), where phase delay maps between pairs of images are inverted into time-series using the redundancy of the measurements. The redundancy is useful to detect unwrapping errors (López-Quiroz et al., 2009) and limits the impact of the decorrelation noise. This approach has also been used successfully for the processing of time-series of displacement from SAR image correlation (Casu et al., 2011).

As opposed to InSAR, this time-series analysis is new for optical imagery. All the previous studies use raw time-series of deformation coming directly from the correlation of images with respect to a given master image (Travelletti et al., 2012; Fahnestock et al., 2015; Lacroix et al., 2015). When multiple images are acquired at the same time (for instance with agile very high resolution (VHR) satellites), averaging the results over the different multiple image pairs reduces the noise (Stumpf et al., 2017). On glaciers, Scherler et al. (2008) filtered the images by taking into account only the correlated images of 1-year apart. Dehecq et al. (2015) smoothed the glacier velocity field and reduced the noise by integrating several deformation fields of Landsat pairs separated by 1-year.

The idea of this study is to use available optical images to derive a system of redundant measurements of displacement fields, to build robust time-series of deformation fields, and to quantify how the network inversion reduces the errors and uncertainties compared to the pairwise process. For that purpose, we adapt the tools developed for InSAR time-series analysis (Doin et al., 2011) to optical data. We then apply these techniques for the long-term monitoring of slow-moving landslides, using the 30 year long SPOT1–5/Pléiades archive, over an area in Peru affected by both earthquakes and rainfalls, with the aim to better understand the relative contributions of these different forcings to the slow-moving landslide kinematics.

2. Study area

The Colca Valley is located in a volcanic area, in southern Peru (Fig. 1). Due to its geological, tectonic and climatic context, the area is propitious to landslides (Lacroix et al., 2015). Indeed, (1) this valley is constituted of successive layers of volcanic, lacustrine and alluvial deposits, incised by a deep river at a rapid rate of 1 mm/yr over the last 0.6 Ma (Thouret et al., 2007), cutting slopes prone for landsliding. (2) The region is subject to seasonal rainfall, with almost all the precipitation falling between December and April (Zerathe et al., 2016) (Fig. 1). (3) The region is seismically very active (Fig. 1) due to volcanic activity (Mw ≤ 3), regional tectonics (Mw ≤ 7; Antayhua et al., 2002), and the subduction of the Nazca plate under the South American plate, 120 km to the West of the Colca Valley (Mw ≤ 8.5; Chlieh et al., 2011).

In this area, nine active landslides were detected using VHR satellites over the 2013 period (Lacroix et al., 2015). These slow landslides affect the same lithologies (lacustrine deposits) and are concentrated over 200 km^2 (Lacroix et al., 2015) (Fig. 1). Among this population, the Maca landslide has extensively been studied (Zerathe et al., 2016). Its volume is estimated to be about 60 to 100 million m^3. It is made of two main blocks, delimited by a near-vertical scarp measuring 15–20 m in height and spreading over 3.5 km long. The block located near the river is the fastest, moving with a mean velocity of 1.5 m/yr over the period of March to July 2013 (Lacroix et al., 2015). The upper block moves slower, with a velocity of 0.8 m/yr on the same period. The Maca landslide kinematics has been studied with GNSS campaigns since 2001 and continuous GNSS since 2012. In particular, two points, one on the landslide, the other on a stable area, were measured 16 times since 2001 (Zerathe et al., 2016). The uncertainty of these measurements is less than 5 cm. These measurements show that the landslide motion is controlled by the seasonal rain (Zerathe et al., 2016) and regional earthquakes (Lacroix et al., 2014). In addition, 11 GPS markers, also located on the Maca landslide, were measured 13 times between November 2011 and June 2014. These in-situ data will be used for validation of the proposed method.

The concentration of landslides in this valley makes the area of large interest for studying the relative contribution of each trigger to landslides dynamics. Indeed all these landslides are submitted to the same pluviometry and same earthquakes (Zerathe et al., 2016). Looking at a group of slow-moving landslides, subject to the same forcings, is an approach that has proven to be efficient for studying the impact of seasonal rainfall (Handwerger et al., 2013), and earthquakes (Lacroix et al., 2015) on slow-moving landslide kinematics. Little is known, however, about the combined effect of these different forcings. The Colca Valley, therefore, offers a great opportunity to study these combined effects over a population of slow-moving landslides.

3. Data processing

The framework for obtaining deformation time-series from optical images is shown in Fig. 2. The processing chain starts with usual steps that are (i) digital elevation model (DEM) generation, (ii) precise orthorectification, (iii) image correlation (Leprince et al., 2007). The novel contribution to the processing strategy here, is to eventually invert all correlation maps into time-series, exploiting the different possibilities that this inversion can offer to improve the signal to noise ratio.
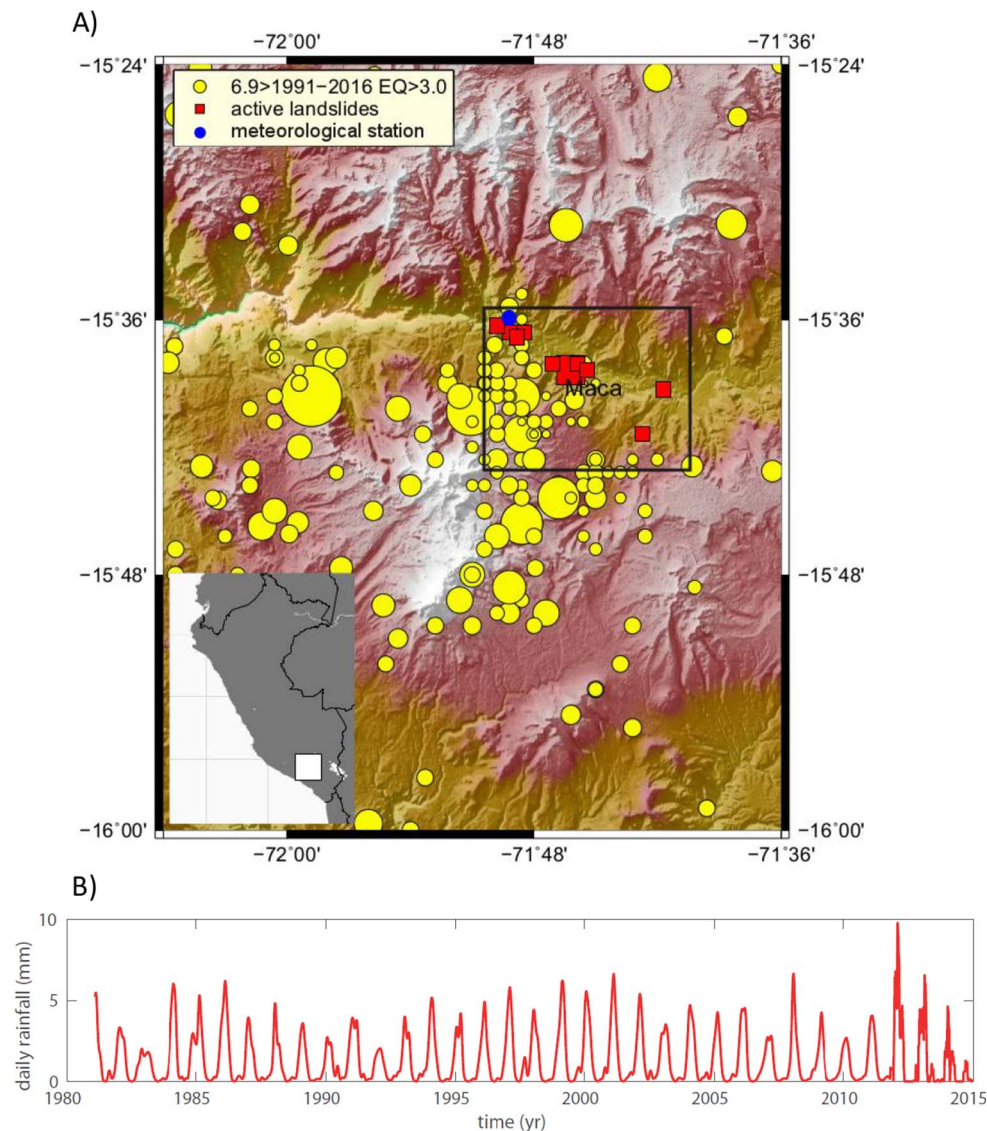
Fig. 1. A) Seismicity map of the Colca Valley for the period 1991–2016, with earthquakes of magnitudes higher than 3. Active landslides detected in Lacroix et al. (2015) are represented with a red square. The black rectangle corresponds to the studied area. B) Time-series of daily rainfall from 1986 to 2015. The meteorological station is located by the blue mark on the map of subplot A). (For interpretation of the references to colour in this figure legend, the reader is referred to the web version of this article.)

3.1. Data

We use 16 cloud-free optical panchromatic images acquired with different satellites between the 15th of June 1986 and the 21st of April 2014. This data set includes 10 images taken from the SPOT 1 to 4 satellites, 2 SPOT5 images, and 4 Pléiades images (Table 1). All these images present large differences of resolution (from 0.7 m for Pléiades image to 10 m for SPOT1–4 images) and image dynamics (coded over 8 bits for SPOT1–4 images, 12 bits for Pléiades images). This data set brings three methodological challenges, that are: (1) the use of images with different resolutions, (2) the low dynamic range of SPOT 1–4 images and (3) the large time span in between images that favours decorrelation due to ground cover changes. Specific solutions adapted to this data set are therefore described in Sections 3.2, 3.3 and 3.5.

3.2. Precise orthorectification

Three precise DEMs with a resolution of 2 m and a vertical accuracy of 0.7 m (Lacroix et al., 2015) are generated with PCI Geomatica thanks to 3 pairs of stereo Pléiades images taken in March 2013, April 2013 and April 2014 (Table 1). These DEMs are used to map-project the

synchronous Pléiades images, using the sensor orientation given by the RPCs. No Ground Control Points (GCPs) were used. This strategy can lead to a constant shift of image georeferencing (Stumpf et al., 2014; Lacroix et al., 2015), which is corrected during the correlation step (cf. Section 3.3).

The 13 monoscopic images are then orthorectified. About 15 tie-points were selected manually on stable areas, between each of the monoscopic images and a reference orthorectified image to estimate the rigorous sensor model in COSI-CORR (Leprince et al., 2007, 2008), that takes into account both the focal plane distortion and orbital errors. The March 2013 image is first chosen as the reference image to orthorectify the 2003 image at a 2.5 m resolution. This image is then used as the reference image for ortho-rectifying the other SPOT images. The tie-points were transformed into GCPs using the orthorectified image and the March 2013 DEM. The GCP's are used to refine the rigorous sensor model given by the satellite ancillary data (Leprince et al., 2007). The image is then orthorectified using the March 2013 DEM, and the obtained rigorous sensor model. Refinement of the GCPs and subsequently the sensor geometry and the image orthorectification is undertaken in COSI-CORR by using an iterative process that compares the orthorectified image around the GCPs and the reference image. This
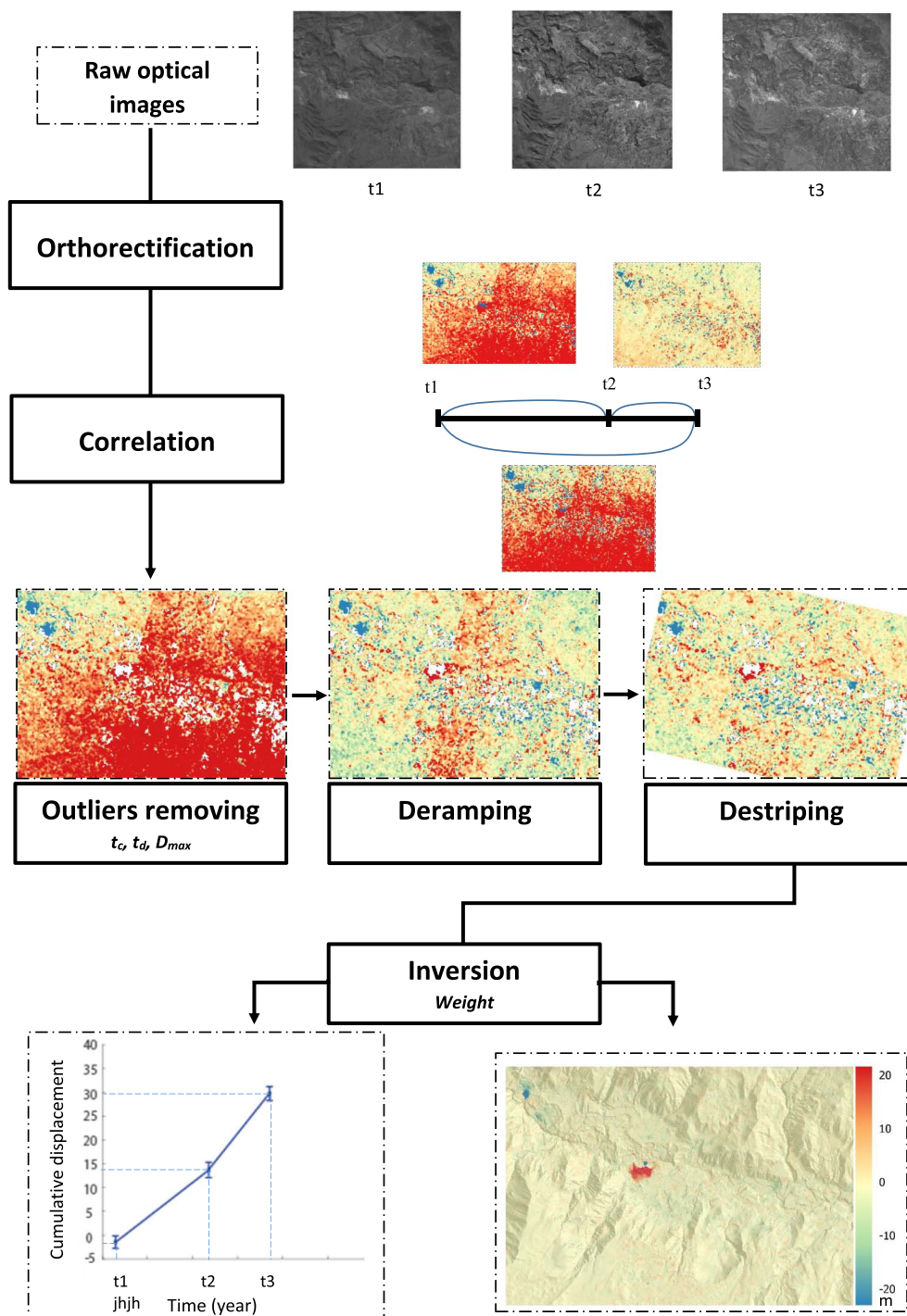
Fig. 2. Processing work flow used to generate displacement time-series of slow landslide over several decades.

comparison is realised over large windows of 256 pixels of 10 m resolution for SPOT1–4 images, to account for large possible changes of the ground cover in between 2003 and the SPOT1–4 acquisitions. The quality of the orthorectification is roughly estimated with the RMS of the difference between the optimised GCPs and the reference image. It is between 1.4 and 2.3 m for the SPOT1–4 images, around 1 m for the SPOT5 images (see Table 1). Resampling of the images is realised at their original resolution thanks to a cardinal sine function with a kernel size of 15 pixels.

3.3. Pairwise processing

Two data sets are created from the 16 ortho-images. The first one, starting in 1986, is based on 16 images re-sampled with a 10 m spacing. The second one starts in 2003 and is based on 6 images with a 2.5 m spacing. When an image resolution was higher than the final data set resolution (e.g. for Pléiades images), we re-sampled them by aggregating all the pixels contained in the final pixel. Inversely, We tried to interpolate all images at 0.7 m. However, this trial was not conclusive for obvious reasons: no information is gained on the 10 m SPOT images by oversampling them, thus the window size during the correlation step (see below) must be increased by a factor of 14 when

Table 1
Parameters of satellite optical images.

Date	Satellite	Across track angle	Along track angle	Resolution (m)	RMSE ortho	Mode	Sun elevation/azimuth (°)
15/06/1986	SPOT1	2.3	9.1	10	1.72 m	Monoscopic	44.0/32.9
08/07/1990	SPOT2	−19.6	8.6	10	1.75 m	Monoscopic	45.4/31.7
14/09/1990	SPOT2	−4.4	9	10	1.83 m	Monoscopic	60.0/52.0
20/10/1996	SPOT3	−25.8	8.5	10	1.66 m	Monoscopic	71.6/76.3
03/07/1998	SPOT2	−25.8	8.5	10	2.30 m	Monoscopic	45.4/30.4
16/11/2000	SPOT4	−26.2	8.2	10	1.81 m	Monoscopic	72.7/103.0
16/04/2001	SPOT4	−19.3	8.4	10	1.90 m	Monoscopic	56.2/42.8
10/06/2001	SPOT1	−18.6	8.7	10	1.76 m	Monoscopic	46.0/29.6
07/10/2001	SPOT2	19.5	9.5	10	2.30 m	Monoscopic	64.0/69.5
16/05/2002	SPOT4	−27.2	8.1	10	1.41 m	Monoscopic	49.9/31.5
21/07/2003	SPOT5	2.3	12.8	2.5	0.92 m	Monoscopic	45.4/36.2
05/05/2010	SPOT5	−13.8	12.5	5	0.98 m	Monoscopic	51.0/36.8
21/03/2013	Pléiades	0.9	−5.8	0.7	−	Stereoscopic	59.3/61.0
15/04/2013	Pléiades	−18.4	3.1	0.7	−	Stereoscopic	55.9/42.9
29/07/2013	Pléiades	2.9	−14.1	0.7	0.45 m	Monoscopic	47.1/38.2
21/04/2014	Pléiades	−11.0	10.7	0.7	−	Stereoscopic	54.0/41.5

oversampling the images from 10 m to 0.7 m, which is not affordable by our processors, and finally we did not get better results.

For the two retained data sets, images are correlated two by two in all possible pairwise combinations and their permutations using the frequency correlator of COSI-CORR (Leprince et al., 2007) with the backward-forward option. This leads to 240 displacement fields at 10 m spacing and 30 at 2.5 m spacing. The COSI-CORR correlator works iteratively in two steps, allowing an iterative refinement of the size windows. To compensate the low dynamics of the 10 m resolution SPOT 1–4 images, a size window of 64 pixels is chosen for the first step of the correlation, before iterating the correlation with a 32 pixel size window for the second step. For 2.5 m resolution images, the size window is directly set to 32 pixels. These values were chosen after a process of trial and errors. Each correlation leads to displacement fields in the E–W and the N–S directions, as well as signal to noise ratio (SNR) maps, estimated by COSI-CORR as a function of the normalized cross-spectrum and a weighting matrix for different frequencies.

3.4. Outliers and bias removal

An editing process is then applied to each displacement field, in order to mask pixels with aberrant displacement values (outliers). Three criteria are taken into account for this mask based on (1) the maximum expected displacement D_{max} in each N–S and E–W direction over the whole period, (here 50 m for the 10 m spacing data set and 20 m for the 2.5 m data set), (2) The quality of the correlation, that is, pixels with SNR lower than a certain threshold t_c are masked, (3) the displacement obtained by the correlation of two images at dates A and B and its opposite (correlation of the images at dates B and A), must have a difference lower than a threshold t_d.

Once this mask is applied, we remove a linear ramp in the displacement fields, caused by possible orthorectification errors (Fig. 2). After this correction, stripes appear, generated by sensor inter-band misalignments (Leprince et al., 2008; Ayoub et al., 2008) that we correct by subtracting the median value of the stacked profile in the along-stripe direction, taking into account only stable areas.

After these processing steps, some noise is still present. It results from a combination of several sources including: (1) DEM errors or change of the topography over 30 years, (2) difference of viewing angles in both acquisitions, and (3) changes of ground cover due to large time spans in between correlated pairs. Hence, the next step has been implemented in order to reduce these errors and uncertainties present in our set of data.

3.5. Time-series inversion

The idea of this step is to use the redundancy of displacement fields to derive a robust displacement time-series for each pixel, together with a noise assessment, in both north–south (N–S) and east–west (E–W) directions separately. In this study, we adapt to optical images a small baseline code designed to be used with InSAR images (Doin et al., 2011). While the adaptation is mostly straightforward, specificities of correlation images must be addressed for increasing the signal to noise ratio.

Considering N optical images, the successive correlation and masking steps lead to a number of correlations varying between $M_{min} \leq M \leq (N-1)N$ for each pixel, depending on the number of pairs where the pixel has possibly been masked. For each pixel, l, we can express the following matrix system:

$$\mathbf{d}^l = \mathbf{G}^l \lambda^l \tag{1}$$

$$\begin{bmatrix} d_1^l \\ d_2^l \\ \vdots \\ d_M^l \end{bmatrix} = \begin{bmatrix} 1 & 0 & \dots & 0 & 0 \\ 1 & 1 & 0 & \dots & 0 \\ \vdots & \vdots & \vdots & \vdots & \vdots \\ 0 & 0 & \dots & 0 & 1 \end{bmatrix} \begin{bmatrix} \lambda_1^l \\ \lambda_2^l \\ \vdots \\ \lambda_N^l \end{bmatrix}$$

where $\mathbf{d}^l$ contains the M displacement measurements for a given pixel, l, and λ^l are the inverted incremental displacements between successive images. $\mathbf{G}^l$ is a MxN matrix containing 1 when the increment λ^l is included in the interval between the two dates of the pair and 0 elsewhere.

To efficiently improve the inverted time-series using the measurement redundancy, we must consider heterogeneities in noise amplitude within the system Eq.(1). We observe first that decorrelation noise increases with time, thus correlation measurements spanning a large duration must be down-weighted with respect to those with a shorter time span. Second, some images systematically yield larger errors in correlation. These images may either be acquired with a different geometry or be affected by a lower image dynamics. Therefore, we define a weight, w_i, for each line, i, of the system Eq.(1), using the standard deviation, σ_i, of each correlation image, i:

$$w_i = \frac{1}{\sigma_i}. \tag{2}$$

The standard deviation is by far dominated by noise as only a very small surface fraction is affected by landslides. It varies with temporal baseline and with the used images, at most by a factor three. This

weight is the same for all pixels of a correlation map. Another source of noise is the large correlation errors (erroneous values outside the main Gaussian noise distribution), that generates patches of erroneous displacements on correlation maps. This will be treated as an additional weight term, pixel dependent, explained below.

The system Eq.(1) weighted with Eq.(2) is solved by a least squares inversion and, in the case of rank deficiency, thanks to an additional constraint on the displacement (López-Quiroz et al., 2009). Rank deficiency occurs when, for a given pixel, l, groups of images are disconnected, i.e., without relative displacement measurements. Here, to compensate this lack of information, we add a minimization constraint on the Laplacian of each pixel time-series. The small weight of these additional constraint lines in system Eq.(1) ensures that only the missing relative displacements are affected by Laplacian minimization. Note that a rank deficiency is less common here than when using InSAR images. Indeed, InSAR images are constrained to tight baseline requirements that might separate data into several subsets (Berardino et al., 2002). This is why the term proportional to the perpendicular baseline described by López-Quiroz et al. (2009) is not included here.

The network misclosure (López-Quiroz et al., 2009) can be quantified by computing for each pixel a residual, R^l, as follow:

$$\mathbf{R^l = d^l - G^l \lambda^l}. \tag{3}$$

R_l is, for a given pixel and a given period, the difference between original measurements and inverted displacements. High residuals highlight correlation values with high bias or low displacement quality and show discrepancy with the other redundant measurements. Including these measurements thus degrade the least square inversion.

To avoid this problem, the inversion is iterated a second time, weighting each measurement, d_i^l, for each pair, i, and each pixel, l, by the residual term, R_i^l, as follow:

$$W_i^l = w_i \times \frac{1}{R_i^{l\,2} + R_0^{\,2}}. \tag{4}$$

where R_0 is a constant that must be approximately equal to the noise standard deviation of "successful" correlations. As a consequence, we set here R_0 to 2 m (see Table 1).

Therefore, the weight, W_i^l, limits the negative impact of strong outliers with very high residuals, but does not artificially overweight correlation values with residuals close to zero.

4. Results

4.1. Spatial analysis

4.1.1. General distribution

Fig. 3 shows the cumulative displacement between 1986 and 2013 given by the inversion of the 10 m spacing data set. This displacement field is dominated by three areas of large displacement (≥ 30 m), that correspond to slow-moving landslides identified on the field and in a previous study using 2013 high-resolution Pléiades images (Lacroix et al., 2015). From East to West, one can identify Maca, Madrigal and Shutone, the three biggest landslides of the area. Elsewhere, the displacement map shows displacement close to 0 with a high variability close to the river and decreasing with elevation. This can be explained by a larger variation of ground cover near the river, linked to the presence of villages and crops, than in altitude, dominated by arid vegetation. As expected, crops and village expansion induce noise in correlation images, however, a few patterns might correspond to smaller landslides as numerous landslides are identified in this area (see Fig. 3 with observed landslides head-scarps from Zerathe et al. (2016) and known landslides from Lacroix et al. (2015)). Among these smaller landslides, two were detected active based on this long-term study, with around 10 m of observed displacement (see the two white dots in
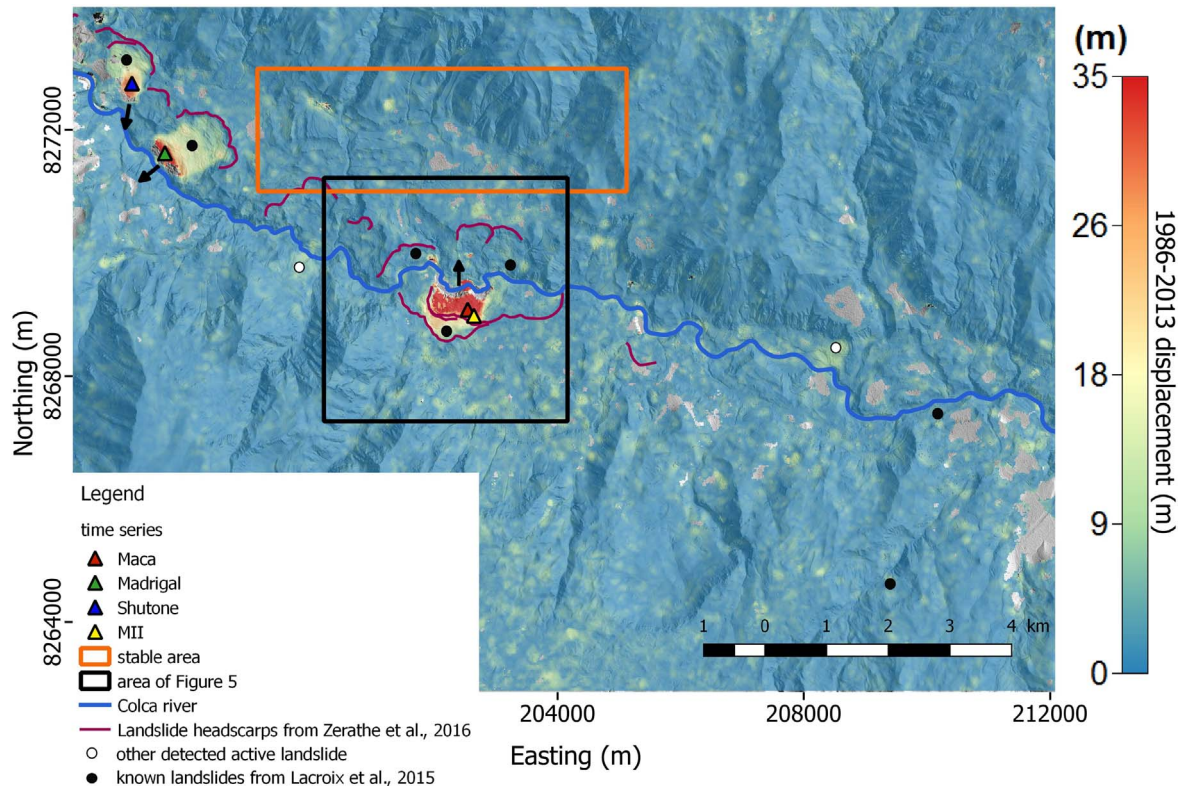

Fig. 3. Map of the cumulative displacement between 1986 and 2013. The displacement direction of the 3 main landslides is indicated with black arrows. Landslide head scarps are mostly from Zerathe et al. (2016), but some were added during this study. Grey patches are pixels with no information due to the mask procedure. (For interpretation of the references to colour in this figure, the reader is referred to the web version of this article.)
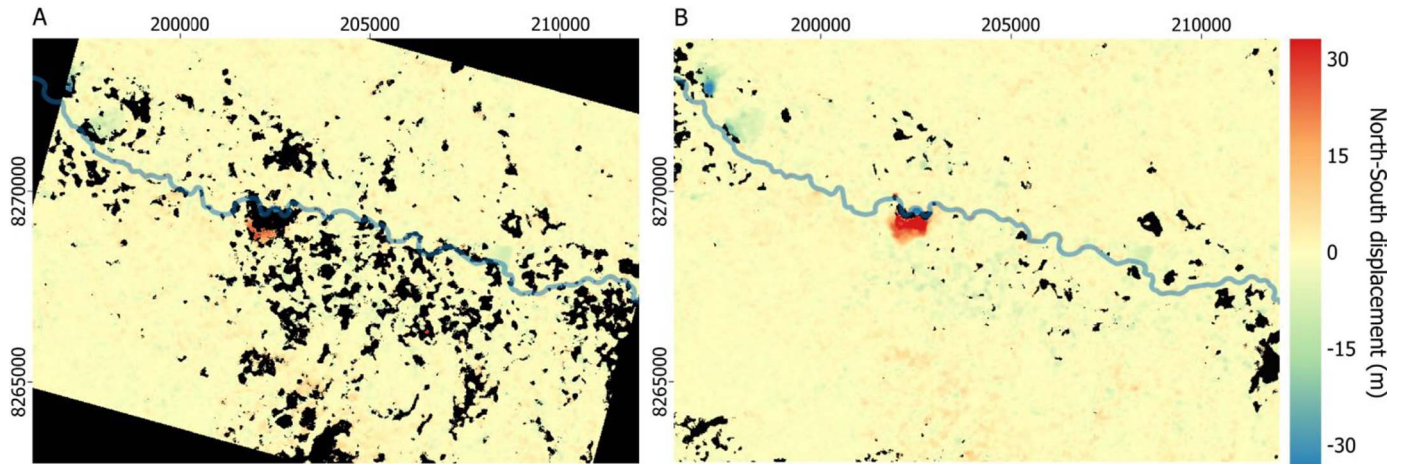
Fig. 4. Maps of the North–South displacement between 1986 and 2013 obtained before inversion (A) and after inversion (B). Positive displacements are North oriented and negative displacements are South oriented. Masked pixels appear in black.

Fig. 3). The one located to the West of Maca was confirmed active thanks to field observations while the one on the East of Maca was not visited.

The three largest landslides are all formed by two blocks, one rapid near the river, and a second, slower, upward (see Fig. 3). This is consistent with field observations and Pléiades measurements (Lacroix et al., 2015). From 1986 to 2013, displacements larger than 35 m and from 10 to 20 m occur in these two distinct landslide sections.

To emphasize the contribution of time-series inversion, we show in Fig. 4, as an example, the north–south displacement over the Maca area between 1986 and 2013 obtained by direct correlation of the two images (A) and by inversion of all correlation maps (B). The comparison shows that the inversion improves the coverage of the measurements. When averaging over the 240 pairs before inversion and the 240 reconstituted pairs after inversion, uncovered areas decrease from 20% to 6%. This shows the high value of the inversion for improving the coverage of the measurements. In particular, we note that the improvement is very large on landslides, where changes of morphology cause strong decorrelation of the signal.

4.1.2. 10 m and 2.5 m data set comparison

We compare the displacements estimated from the 10 m and 2.5 m data sets over the same period of time, from 2003 to 2013. Fig. 5 shows a zoom of the N–S displacement estimated over an area affected by several landslides including Maca. On the two maps, the Maca landslide is composed of two main blocks separated by a scarp, with similar values of displacement for the two maps. However, we can also notice large differences at the limits of these blocks and on the banks of the river. For instance, the limits of the two blocks coincide with the scarps in the displacement fields at 2.5 m spacing, but not at 10 m spacing. This can be explained by the smoothing induced by the different window size used by the correlator, 320 m and 80 m for the 10 m and the 2.5 m data sets, respectively (see Fig. 5).

A strong discrepancy between both maps occurs near the river, where displacements have opposite directions for the two data sets, as shown in areas encircled in Fig. 5. We interpret this observation by the lower texture and dynamic range of 10 m spacing images that enhance the correlator sensitivity to large objects with large contrasts, like the river/bank contrast. Therefore, with 10 m spacing images, the correlator is sensitive to the motion of the riverbed, going southwards as
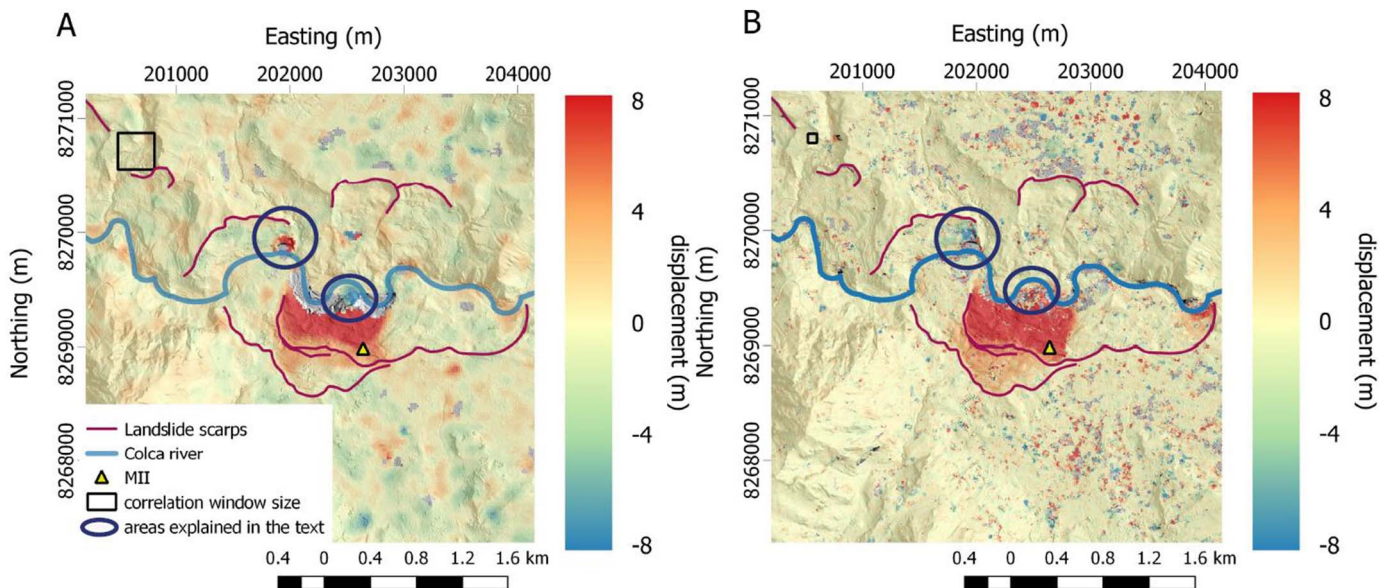

Fig. 5. Maps of the North–South displacement between 2003 and 2013 for the Maca landslide obtained thanks to (A) 10 m spacing image correlations, (B) 2.5 m spacing image correlations. Positive displacements are North oriented and negative displacements are South oriented. Scarps are from Zerathe et al. (2016). Masked pixels appear in grey. Correlation windows are 320 m wide in (A) and 80 m wide in (B).

erosion proceeds at the toe of the Maca landslide. For the 2.5 m spacing images, the correlator is sensitive to finer texture like crops and walls limiting the crops. This phenomenon appears restricted to scattered areas near the river and eventually, we are confident on results obtained by inversion on large areas of homogeneous velocities, e.g. when located in central parts of large landslides.

4.2. Uncertainties estimation

We estimate uncertainties in the displacement fields by calculating the standard deviation of a stable area (orange square, Fig. 3). This area of 12 km² is chosen between the three main landslides, encompassing a zone covered by agricultural fields and villages. After inversion, depending on pairs, the uncertainty varies between 0.7 and 2.6 m for the 10 m spacing data set(Fig. 6A) and between 0.49 and 1.43 m for the 2.5 m spacing data set(Fig. 6B). In the case of the first data set, some dates come out with stronger uncertainties as, for example, the dates 10/1996 and 11/2000. It is also interesting to notice that pairs of SPOT5 and Pléiades images have globally a lower uncertainty than SPOT1–4 pairs. Regarding the 2.5 m data set(Fig. 6B), it seems that the uncertainty is mainly coming from the oversampling of the image acquired in 2010.

In order to have a better understanding of the inversion impact on the uncertainties computed on the stable area, we computed the relative changes between the standard deviation before and after the inversion for each pair (Fig. 6C and D). Inversion reduced on average

the standard deviation by 13 and 21% for the two data sets. However, the improvement is larger for specific pairs, mostly the ones that came out with larger uncertainties in Fig. 6A and B. In addition, it appears that among these pairs, the inversion had a bigger impact on pairs separated by a larger time span, this mostly being visible in Fig. 6C. Indeed, the improvement reaches 18% for the 2.5 m data set and more than 30% on average for the 10 m data set.

Furthermore, the noise amplitude is dependent on the ground cover, slope, texture, etc., and thus varies geographically. As a consequence, the number of pairs available after applying the masks varies spatially and can be used as a proxy for defining the spatial variation of the inversion uncertainties. The noise standard deviation is thus computed for pixels in the stable area containing the same number of available pairs. This is done for each date separately and for both 10 m and 2.5 m spacing data sets(Fig. 7). Finally, we display the standard deviation averaged over all dates, together with the maximum and the minimum standard deviation of all dates(Fig. 7A and B). These two plots reveal that the noise amplitude decreases as the percentage of pairs used in the inversion increases, e.g., the local correlation quality increases. This improvement is particularly significant as soon as at least 40 to 60% of pairs are available.

We also notice that the 2.5 m spacing data set has high uncertainties when more than 60% of the pairs are masked. We explain this with 2 effects: (1) the 2.5 m data set was processed with window size of 32 pixels directly whereas the 10 m data set was processed with a first step at 64 pixels before a second step at 32 pixels (see Section 3.3) and
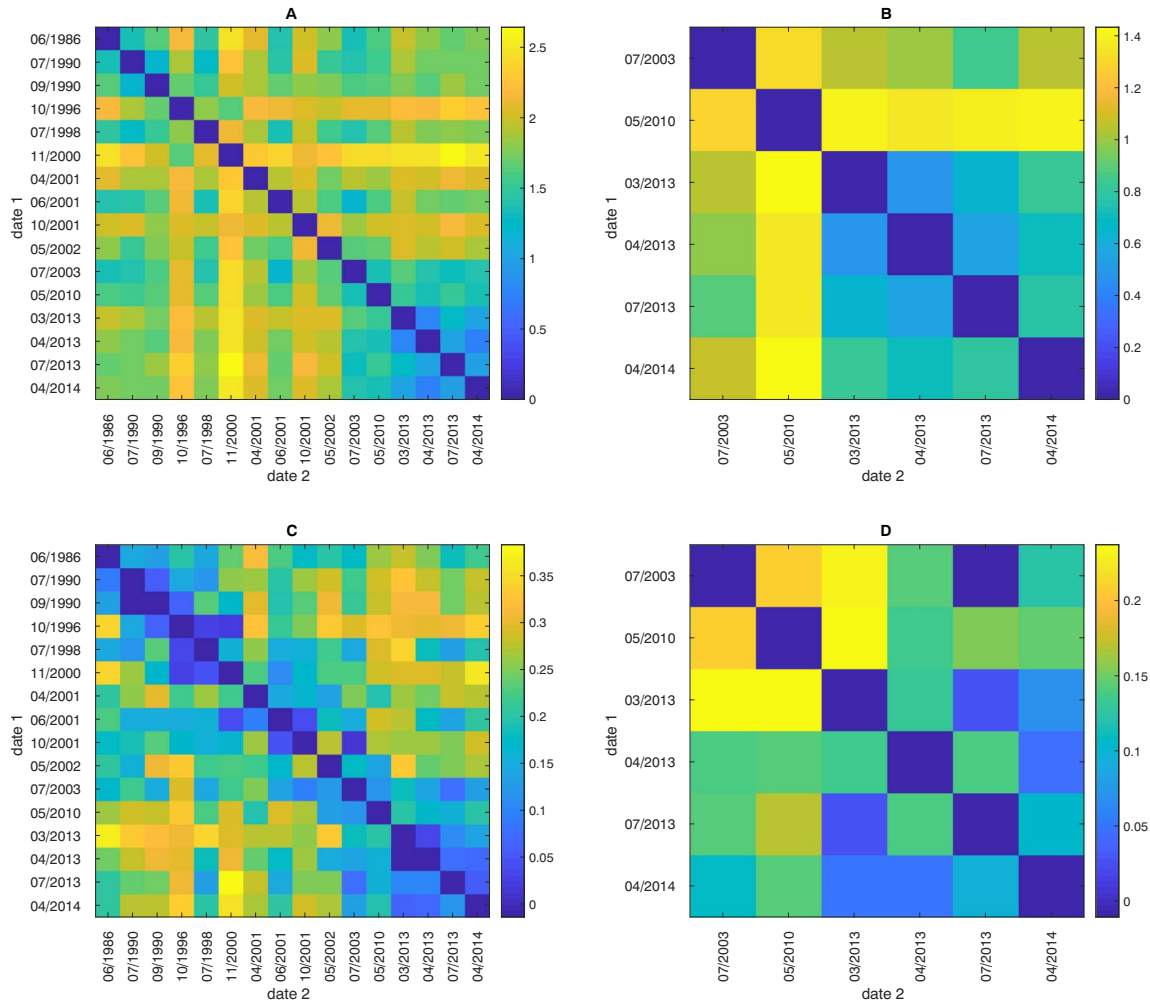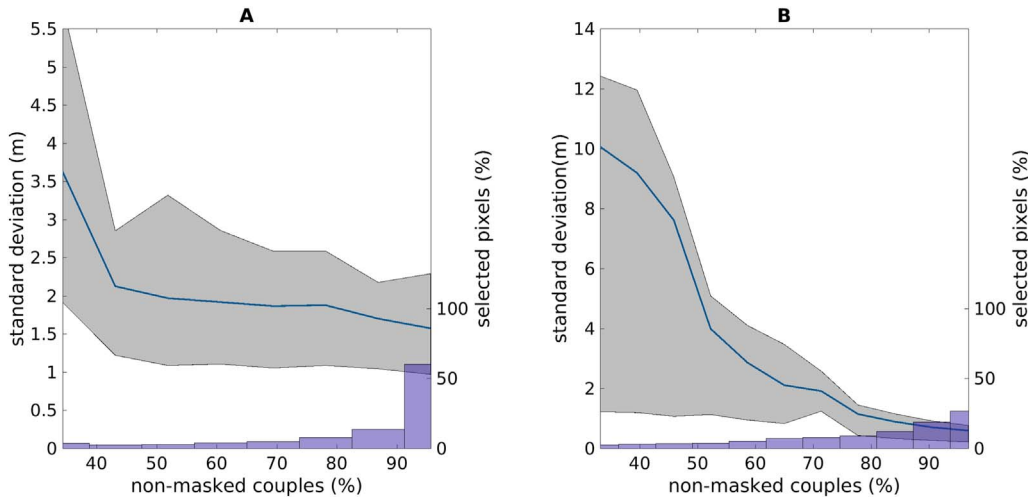

Fig. 6. Standard deviation in meters of the stable area on the 240/30 pairs after inversion (A) for the 10 m resolution data set (B) and the 2.5 m data set. Variance reduction in meters between the standard deviation of the stable area on the 240/30 pairs before and after inversion (C) for the 10 m resolution data set and (D) the 2.5 m data set.

Fig. 7. Mean uncertainty over each date as a function of pairs available for inversion (A) for the 10 m resolution data set and (B) for the 2.5 m resolution data set. The maximum and the minimum standard deviations over every date are represented by the shaded area. The histogram represents the percentage of selected pixel of the stable as a function of non-masked pairs. the standard deviation is calculated from these selected pixels.

(2) the 2.5 m contains much more details, that can evolve strongly through time, whereas the 10 m data set is mostly constituted by large objects stable with time. The relationship between the standard deviation and the percentage of non-masked pairs for a given pixel and a given date will be used in the following as a proxy to define the spatial variation of the inversion uncertainties.

4.3. Time-series analysis

In order to evaluate how correlation redundancy and inversion improve retrieved displacement time-series, we compare the displacement time-series of the 2 data sets at the validation GPS points, 12 in total, widespread on the Maca landslide with GPS measurements. Among these 12 GPS markers, 11 were installed in 2011 and measured 13 times between 2011 and June 2014. The last GPS marker, the point MII (see Fig. 3), was installed in 2001 and measured 14 times between 2001 and 2014.

4.3.1. Study of the point MII

First, we compare the time-series obtained with inversion to the time-series that would have been obtained without inversion at 10 m spacing at the location of the point MII (see Fig. 3). For non-inverted time-series, we tested two different approaches. The first one consisted in generating 16 forward time-series, each having a different reference date, and with displacements given directly by the correlation between the references and all the other dates (see time-series ' without inversion' in Fig. 8). The second time-series is built by adding the displacements of consecutive pairs (see the time-series ' with consecutive pairs' in Fig. 8). Overall, with the first method, non-inverted time-series show similar trends of displacement but differ in amplitude. Among these non-inverted time-series, some tend to diverge from the inverted one, especially when the time interval between correlated images increases. In addition, every time-series obtained before inversion should have 16 different points corresponding to each acquisition date. Yet, some time-series have masked values due to the applied masks described in Section 3.4. It appears that the number of masked pixels is larger as we get closer to the two extremities of the time-series. At this specific location, i.e. the point MII, these two observations highlight a strong decorrelation with time. Furthermore, these 16 non-inverted time-series depend on an arbitrary choice for the reference date.

The time-series obtained by using only consecutive pairs is very similar to the inverted one, with a smaller amplitude around 2013–2014. However, for this method, the uncertainties and the bias will increase with the succession of time increments. The inversion method provides two advantages: time-series with limited gaps due to decorrelation with time, and a robust result by optimally combining all
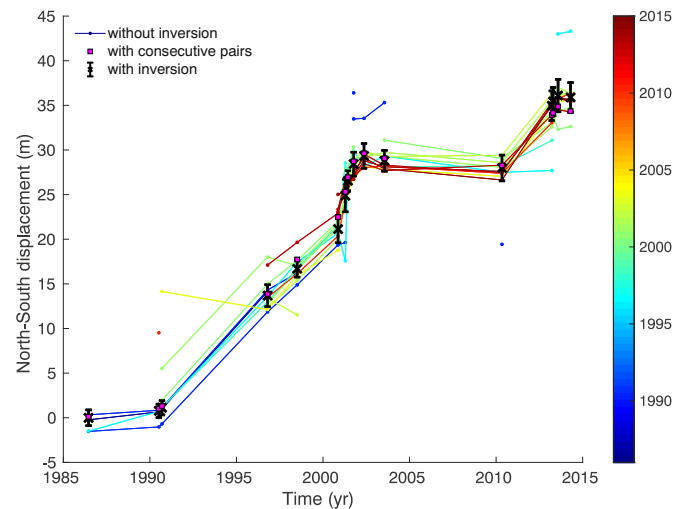
Fig. 8. Comparison of 3 different computational strategies to generate cumulative displacement time-series at the GPS point MII (see location Fig. 3). For time-series build without inversion see details in Section 4.3.1. The line's colours refers to the reference date. Each time-series computed without inversion was displayed by removing the mean of the differences between the inverted and the non inverted displacements. The black crosses represent the time-series obtained after inversion (see Section 4.2 and Fig. 7 for errorbars computation). (For interpretation of the references to colour in this figure legend, the reader is referred to the web version of this article.)

time-series correlations, hence reducing the noise.

Finally, we quantify the associated uncertainties of the inverted time-series of displacements by comparing the GPS time-series available at point MII (Figs. 3 and 5) with inverted time-series at 2.5 and 10 m spacing over the period 2001–2014, common period to the three time-series in both N–S and E–W directions (Fig. 9A and B). In order to be comparable, we aligned the time-series on the 2013–2014 period, corresponding to a stable stage for the landslide.

The N–S direction of the GPS time-series (Fig. 9A), the main direction of the Maca landslide, shows that the landslide stayed stable for at least 7 years starting in 2002 and then accelerated, with 10 m of displacement reached in 2 years. Eventually, from 2013 to 2014, the Maca landslide stayed stable again. Basic trends of time-series after inversion are coherent with the GPS time-series. The standard deviation of the difference between the inverted time-series and the interpolated GPS time-series at the date of the optical images are, in the N–S direction, of 2.3 m and 0.5 m are formed for the 10 m and the 2.5 m data sets, respectively, corresponding to about 1/5 th of the pixel resolution. In the E–W direction, the error is slightly lower, with
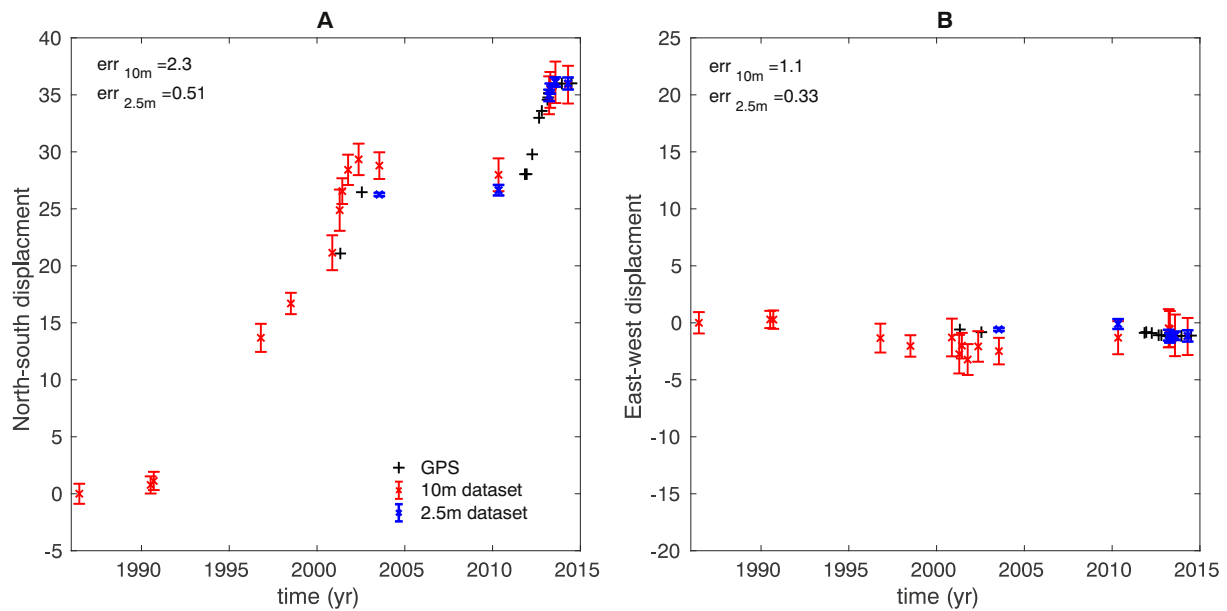
Fig. 9. Time-series obtained by inversion of 10 m and 2.5 m spacing image correlations, compared with GPS time-series at point MII (see location in Fig. 3) in (A) the North–South and (B) the East–West directions. Errors indicated in the left corners of (A) and (B) correspond to the standard deviation of the difference between the inverted time series and the interpolated GPS time series at the date of the optical images. See Section 4.2 and Fig. 7 for error bars computation.

a value of 1.1 m and 0.33 m for the 10 m and the 2.5 m data sets, respectively.

While the 10 m resolution time-series has, overall, a lower displacement amplitude than measured by GPS, the 2.5 m resolution time-series is in very good agreement with the GPS. This difference is explained by the location of the GPS near the landslide limit (Fig. 5) and the smoothing introduced by a larger correlation window size in the case of 10 m spacing time-series compared to 2.5 m spacing time-series.

4.3.2. GPS and inverted time-series comparison

We also use the 11 other GPS time-series acquired between 2011 and 2014 (Zerathe et al., 2016) to estimate the errors of the satellite time-series on a shorter time-scale, i.e. 3-years, and to observe how these errors vary in space. For that, we interpolate the 11 + MII GPS time-series at the 4 optical image dates from March 2013 to April 2014. Then, for each GPS marker, we compute the standard deviation of the differences between the 4 interpolated GPS displacements and the inverted time-series. This leads to 12 values of standard deviations, both in N–S and E–W directions and for both 2.5 m and 10 m spacing data sets. The maximum and the mean standard deviation of the 12 measurements are summarized in Table 2.

The mean standard deviation is of 39 cm in both N–S and E–W directions for the 10 m spacing data set and around 20 cm for the 2.5 m data set. This is better than errors found with the point MII on a longer time-period but of the same order than standard deviations computed on the stable area with only Pléiades images (see Fig. 6), corresponding to the images used in this comparison.

Table 2
Difference between the 12 GPS time-series and their corresponding inverted time-series, in the NS and EW directions and for the two data sets. See Section 4.3.2 for more information.

	10 m		2.5 m	
	NS	EW	NS	EW
Mean (m)	0.39	0.39	0.22	0.17
Max (m)	1.03	0.60	0.39	0.34

5. Discussion

5.1. Contribution of the inversion method

Displacement uncertainties have been shown to depend on various sources, including (1) DEM accuracy, (2) difference in viewing angle between two acquisitions, (3) image resolution, (4) coherence between two successive images and (5) difference of illumination (Stumpf et al., 2016). In our case, uncertainties come, inter alia, from decorrelation with time due to large time spans in between correlated images and land cover changes generating false displacement. The decorrelation sometimes leads to strongly erroneous displacement values that are masked after the correlation step (see Fig. 8). Applying directly the correlation to acquisitions with large temporal separation leads to gaps in cumulative displacement maps and times-series, whereas the inversion reduces significantly these gaps, from 20% to 6% (see Fig. 4).

We investigated the origin of the higher uncertainties, that can be observed on certain dates (Fig. 6). We looked at the effect of illumination (i.e. sun elevation and azimuth) on the uncertainties for the 10 m data set only. We found that the uncertainty in the N–S direction is strongly correlated to the difference in sun elevation/azimuth between images (Fig. 10), this effect being less prominent on the E–W component. Nevertheless, the inversion contributes to decrease uncertainties in both directions.

The impact of illumination is especially a problem when correlating images acquired in mountainous area. Two strategies can be undertaken to reduce the uncertainties from illumination: (1) selecting pairs only of similar illumination as done by Dehecq et al. (2015), and (2) weighting the pairs as a function of their sun elevation differences.

Previous studies using 10–15 m resolution images displayed displacement uncertainties around 1/4 th to 1/10th of the pixel size, for study durations varying between 1 month and 3 years (Van Puymbroeck et al., 2000; Michel and Avouac, 2002; Leprince et al., 2007; Taylor et al., 2008; Scherler et al., 2008; Heid and Kääb, 2012). For the same resolution, we retrieve after inversion similar uncertainties, around 1/ 5th to 1/ 6th of the pixel size, but for a study duration at least ten times longer.

Concerning the 2.5 m data set, the noise amplitude after inversion varies mainly between 1/2 and 1/ 4th of the pixel size (Fig. 7). Previous studies using 0.5 to 2.5 m resolution images found lower uncertainties,
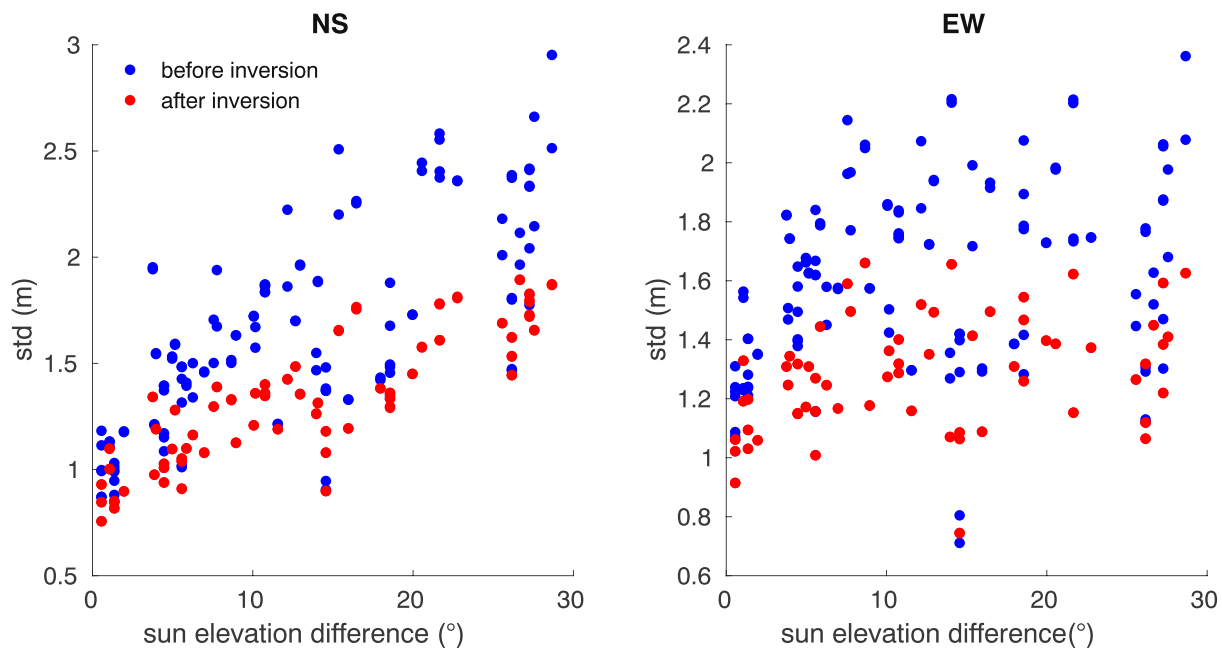
Fig. 10. Standard deviation in displacements of the stable area (see Fig. 3) as a function of the difference of the sun elevation between correlated images for the 10 m data set.

varying from 1/ 4th to 1/ 8th of the pixel size (Berthier et al., 2005; Binet and Bollinger, 2005; Stumpf et al., 2014; Lacroix et al., 2015). However, these studies were carried on very short durations, from 1 to 6 months. Delacourt et al. (2004), using Quickbird and aerial images with a resolution of 1 m for studying a region over 4 consecutive years, had uncertainties around 3.6 m on average. This uncertainty is largely above our noise amplitude even though we are studying a period of

11 years with 2.5 m spacing images.

5.2. Control of the landslide kinematics

We notice side effects due to large correlation window size, smoothing the measured displacement near landslide limits. In the following, we avoid this bias by selecting points located within blocks
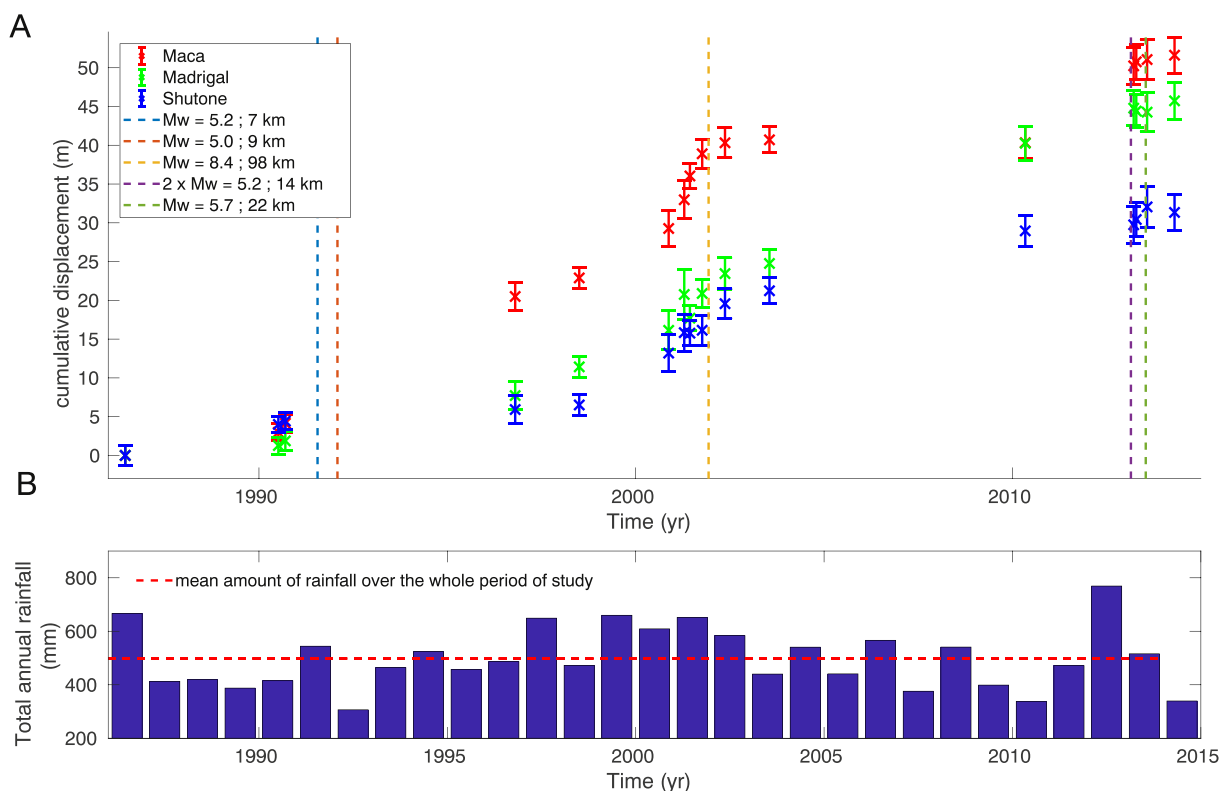

Fig. 11. A) Cumulative displacements of Maca, Madrigal and Shutone in their rapid zone. Large earthquakes, whose effect was largely felt in the area, are represented with vertical dashed lines. Their moment magnitude together with the distance between their epicentre and Maca are indicated in the legend. See Section 4.2 and Fig. 7 for errorbars computation. B) Cumulative rainfall per year from Zerathe et al. (2016).
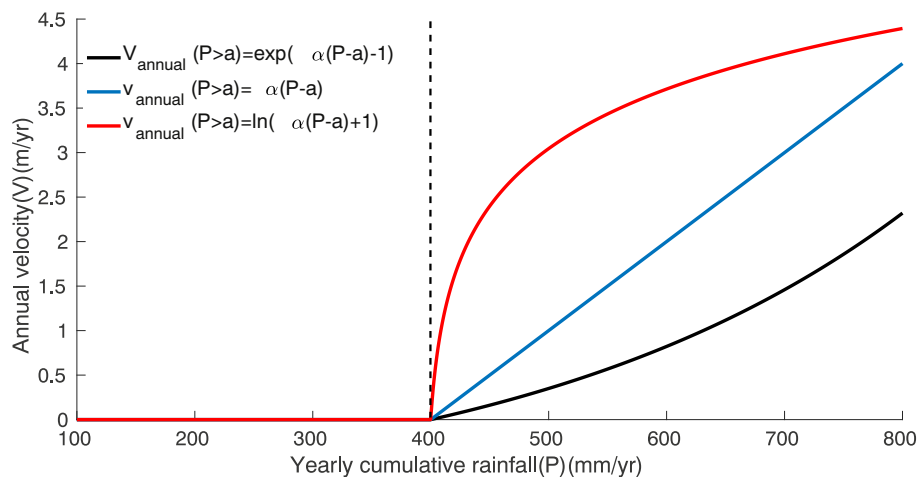
Fig. 12. Functional form of the three different hydro-mechanical models (cf. Section 5.2).

of homogeneous movement and checking the pixel choice by confronting 10 m to 2.5 m spacing displacement results. For a given pixel, we compute the regression coefficient between the two data sets, and extract only points with a regression coefficient close to 1 ± 0.1 and with relative discrepancies within error bars defined for each pixel and date.

Three locations were selected on the fast zone of the three biggest landslides of the studied area that are Maca, Madrigal and Shutone (see location in Fig. 3). As visible on Fig. 11, from 1986 to 2014, Maca and Madrigal underwent up to 50 m of displacement and Shutone around 35 m. The three time-series display monotonic displacements with time, modulo the uncertainty. These three landslides present acceleration and stability phases and we observe that those phases differ from one landslide to another. For example, between 1990 and 1998, the Maca landslide underwent a strong displacement while Madrigal and Shutone only moderately moved. A difference in landslide response is also visible between 2003 and 2010 where Maca underwent no displacement (this is confirmed by GPS time-series) whereas Madrigal and Shutone experienced around 13 and 8 m of displacements, respectively.

The three landslide kinematics seem to respond to dry and rainy episodes. This is visible especially between 1998 and 2002 where each studied landslide underwent large displacements, in reaction to several years of strong rainy seasons. This is coherent with a previous study from Zerathe et al. (2016) carried between 2001 and 2014 on Maca, indicating that its motion is mainly controlled by rainfall, and triggered only when a certain amount of cumulative rainfall per year is reached. However, Fig. 11 shows that for the same amounts of yearly cumulative rainfall, Maca either underwent large displacement (e.g. between 1991 and 1996) or very little displacement (e.g. between 2002 and 2011).

We test three different and simple statistical hydro-kinematical models in order to gain insight on mechanisms impacting the kinematic of these three landslides. The input precipitation is homogeneous over the valley at the seasonal scale (Zerathe et al., 2016) and hence is the same for the three landslides. In order to stay simple, and due to the limited number of time-intervals in the time-series, these three models are composed of only two parameters. The first parameter a controls the precipitation threshold to initiate a landslide motion (Van Asch et al., 1999; Zerathe et al., 2016). The second parameter, α, controls the annual velocity to the landslide as a function of the yearly precipitation. This α parameter is either used in a purely empirical linear law (Zerathe et al., 2016), a logarithmic or an exponential law (see Fig. 12). In addition to being simple, the logarithmic and exponential relationships allow, in a schematic way, to represent the displacement of a sliding block submitted to rate and state friction law (Chau, 1995; Helmstetter et al., 2004; Lacroix et al., 2014; Handwerger et al., 2016). The logarithmic law suggests a rate-strengthening interface of the sliding

Table 3
Coefficients that best fit the difference between modelled and measured displacements together with obtained RMSE for the three different landslides and the three different models.

Model	Parameters	Maca	Madrigal	Shutone
Linear	a (mm/yr)	377	398	472
	α	0.015	0.014	0.018
	RMSE	4.13	1.8	1.54
	LOOCV error	4.69	2.11	1.82
Logarithmic	a (mm/yr)	610	487	542
	α	385	0.34	0.53
	RMSE	3.79	1.41	1.65
	LOOCV error	4.14	1.65	1.81
Exponential	a (mm/yr)	200	215	326
	α	0.0031	0.0033	0.0038
	RMSE	4.82	1.39	1.74
	LOOCV error	6.46	3.91	2.62

surface, which would less likely fail in a catastrophic way. On the contrary, the exponential law represents a slow-moving landslide constituted of rate-weakening materials that might evolve toward a flow (Handwerger et al., 2016). However, it is important to highlight that the inverted parameters are purely statistical and that their physical meanings encompass the effects of rheology, geometry, hydrology, on the landslide kinematics. Only a has a direct physical meaning about the landslide motion initiation.

The threshold a and the triggered amplitude α were found by minimizing the difference between inverted displacement and the model, using the L2 norm and the annual precipitation as an input. A grid search provides an initial solution for an optimisation based on the Nelder-Mead simplex algorithm. Obtained values of a and α are gathered in Table 3 together with the final RMS residual. To check the predictability of the displacements obtained with the model and hence, the error of the model, we apply a leave-one-out cross-validation (LOOCV) (Efron and Gong, 1983). The error of the model is defined as the root mean square of the differences between the modelled displacement and the inverted displacements removed for the LOOCV (see LOOCV error in Table 3).

The RMSE and LOOCV error of each 9 cases (Table 3) show that, globally, the logarithmic model fits better Maca and Madrigal inverted time-series. Shutone is well fitted by both linear and logarithmic models with a LOOCV error very similar but a RMSE lower for the linear model. The logarithmic model fitting well our data is in agreement with Lacroix et al. (2014), where they found that the Maca landslide follows a rate-strengthening law.

Nevertheless, it is interesting to notice that whatever the model
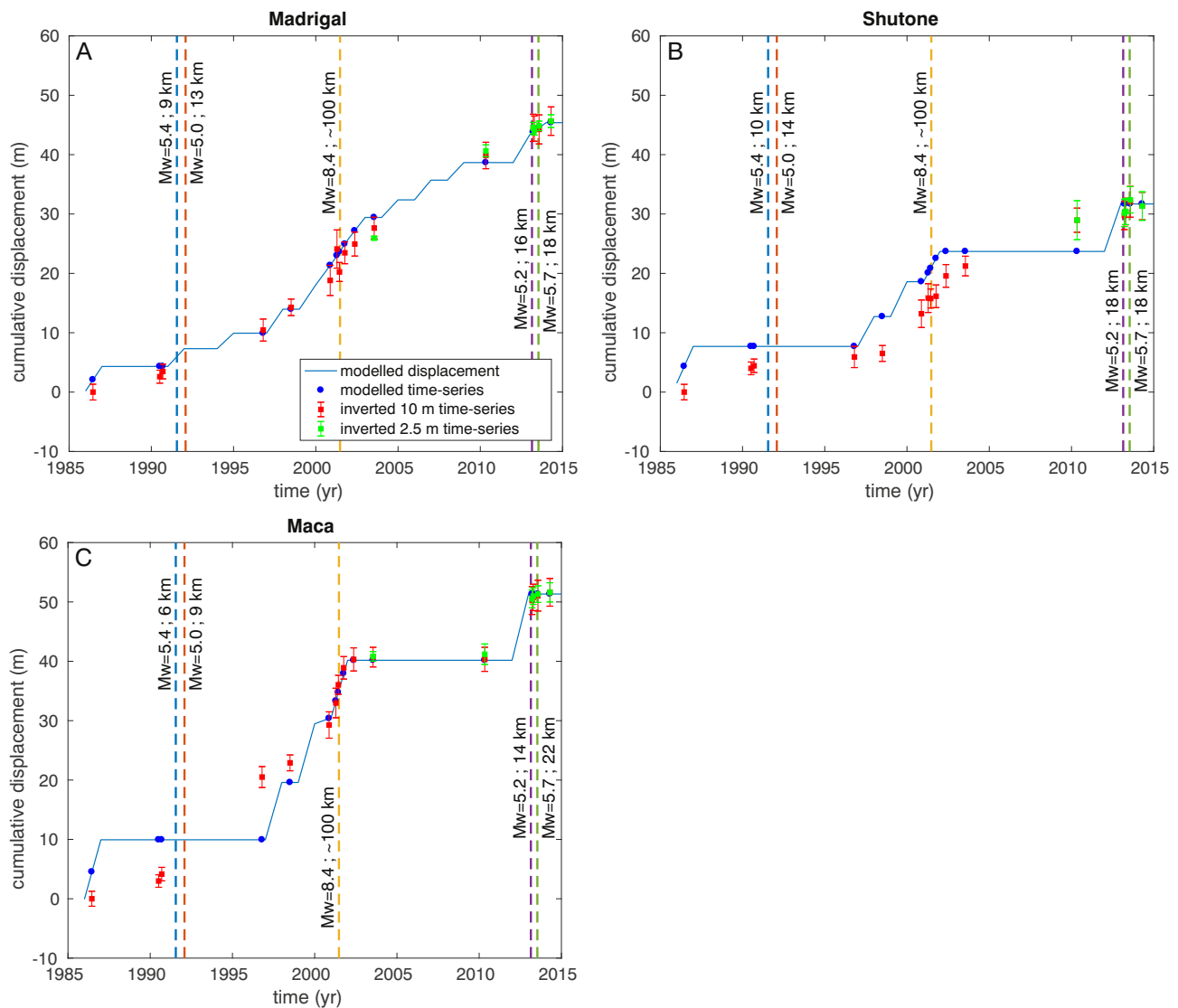
Fig. 13. Cumulative displacement obtained by inversion of the 10 m data set (red) for the Madrigal (A), Shutone (B) and Maca (C) landslides. In blue are plotted the best fits of the logarithmic models (see scheme in Fig. 12). Dashed lines correspond to earthquakes that could possibly impact the landslide kinematics together with their magnitude and the distance to the concerned landslide. (For interpretation of the references to colour in this figure legend, the reader is referred to the web version of this article.)

used, the RMSE and the LOOCV error are consistently at least twice higher for Maca than for Madrigal and Shutone. To better understand these high values, we plot the displacements obtained with the logarithmic model, which fits the best the three landslide kinematics and compare them to the inverted displacement time-series of Madrigal, Shutone and Maca (see Fig. 13).

Fig. 13 (A) and (B) shows that the models fit fairly successfully measured displacements on Madrigal (A) and Shutone (B), with some errors possibly due to the simplicity of the statistical model and the fact that the models don't take into account the impact of successive years of high precipitation or drought (Bennett et al., 2016). It is also interesting to note that the displacement on the Maca landslide (C) is well fitted only at two different periods: after 2000, as well visible in Fig. 13 (C), and prior to 1991. Between June 1986 and September 1990, the model and the observations are not overlapping due to a reference choice. Nevertheless, the predicted displacement for this time period is of 5.4 m, which is comparable to the actual 4.2 m ± 2.4 m measured thanks to optical images on the same period. However, between 1991 and 2000, the model and the observations are very different and even contradictory. High modelled displacements are found when the landslide is actually not or very slowly moving, whereas stability is

modelled when the landslide is actually undergoing strong motion. Yet, two local earthquakes of *Mw* 5.4 and 5.0 strongly affected Maca in 1991 and 1992 (Antayhua et al., 2002). The 1991 earthquake destroyed the church of Maca, killed 14 inhabitants, and strongly impacted the landslide (Bulmer et al., 1999). Other areas (Madrigal and Shutone) were much less affected by the local earthquake. This shows that ground motion was certainly much lower in Madrigal and Shutone than in Maca. A simple modelling of the peak ground acceleration (PGA) for a soft soil (Akkar and Bommer, 2010) taking into account the source location uncertainty (Antayhua et al., 2002), shows that the PGA can be lowered by 36% between Maca and Madrigal and 46% between Maca and Shutone. This highlights the rapid decay of the ground motion with distance for such magnitude 5 earthquake and, as a consequence, explains the observed behaviour of Maca and other landslide kinematics in the 1990s. Therefore, we suggest that the large motion observed between 1990 and 1996 on the Maca landslide (16 m of displacement), while annual rainfalls were low, might be due to this specific earthquake, as it can't be explained by hydrological events only. Due to the data set sparsity, it is however difficult to know if the 16 m are only co-seismic. It is highly probable that this motion includes post-seismic motion either due to variations of the landslide basal friction properties

(Lacroix et al., 2014) and/or complex interaction with post-seismic rainfalls due to damage of the landslide body as seen in the case of rapid triggered landslides (Marc et al., 2015).

Regarding the other earthquakes plotted in Figs. 11 and 13, they were all located at a higher distance to the landslides compared to the 1991 earthquake and for similar magnitudes. Thus, we believe their impact was certainly not null on the landslide kinematics, but at least not measurable by our 10 m resolution optical images. By comparison, the 2013 Mw 5.7 earthquake accelerated the Maca landslide by 8 cm in 5 weeks, the landslide being located 20 km away from the source (Lacroix et al., 2014).

Finally, we hypothesise that the small displacement observed between 1996 and 1998 on the Maca landslide, when precipitation were high, might be a secondary effect of the 1991 earthquake (Fig. 11). Indeed, the landslide underwent strong displacements between 1991 and 1996 that might have been slowed down by an asperity on the slip surface (i.e. bumps, broad steps and depressions), despite a large amount of precipitation. Basal geometry has already been evoked to explain the temporal variability of landslide kinematics (Baum and Johnson, 1993). This could explain the observed kinematics of the landslide after the 1991 earthquake. We want to emphasize that the several years of strong precipitation might have also played a role in the acceleration that the Maca landslide underwent after 1998 (Bennett et al., 2016).

6. Conclusions

We adapted a method that allows us to generate displacement time-series from optical images correlation. The main benefit of this method is the possibility of generating long time-series of several years to decades while keeping uncertainties similar to previous shorter duration studies. Moreover, uncertainties are also reduced for images separated by short periods of time. Therefore, this method is also interesting for the present time, with an important number of images freely available, e.g. with the Sentinel-2 or Landsat-8 programs that provide acquisitions for a given area every few days. The proposed method can indeed be used to build robust time-series of landslide displacements and analyse their transient signals for a better understanding of these mass-movement dynamics. The use of Sentinel-2 images instead of SPOT1–5 images will certainly provide better results as images are always acquired with the same geometry. Implementation of the method on the Geohazard Exploitation Platform (GEP) of the European Space Agency (ESA) is under progress for that purpose.

The obtained 28-year long time-series allows us to discuss the impact of the precipitation and earthquakes on the kinematics of three landslides in the Colca Valley, Peru. Precipitation is the main forcing controlling their displacement with time. We propose simple models relating precipitation to motion, with a threshold effect of precipitation on the landslide behaviour. Our analysis also highlights a possible strong impact of a local Mw 5.4 earthquake, in 1991 on the kinematics of the Maca landslide. Its effect might have been double, with an acceleration of the motion of the landslide during the co- and post-seismic periods(< 6 years) and a modification of the material properties (damage) that can lead to complex interactions with rainfalls and enhance the landslide movements.

Acknowledgments

References

Akkar, S., Bommer, J.J., 2010. Empirical equations for the prediction of PGA, PGV, and spectral accelerations in Europe, the Mediterranean region, and the Middle East. Seismol. Res. Lett. 81 (2), 195–206.

Antayhua, Y., Tavera, H., Bernal, I., Palza, H., Aguilar, Victor, 2002. Localización hipocentral y características de la fuente de los sismos de Maca (1991), Sepina (1992) y Cabanaconde (1998) región del volcán Sabancaya (Arequipa). Bol. Soc. Geol. Peru 93, 63–72.

Ayoub, F., Leprince, S., Binet, R., Lewis, K.W., Aharonson, O., Avouac, J.P., 2008. Influence of camera distortions on satellite image registration and change detection applications. In: IGARSS 2008 — 2008 IEEE International Geoscience and Remote Sensing Symposium. vol. 2 pp. II-1072–II-1075.

Baum, R.L., Johnson, A.M., 1993. Steady movement of landslides in fine-grained soils: a model for sliding over an irregular slip surface. In: Landslide processes in Utah observation and theory bulletin 1842.

Bennett, G.L., Roering, J.J., Mackey, B.H., Handwerger, A.L., Schmidt, D.A., Guillod, B.P., 2016. Historic drought puts the brakes on earthflows in Northern California. Geophys. Res. Lett. 43 (11) 2016GL068378.

Berardino, P., Fornaro, G., Lanari, R., Sansosti, E., 2002. A new algorithm for surface deformation monitoring based on small baseline differential SAR interferograms. IEEE Trans. Geosci. Remote Sens. 40 (11), 2375–2383.

Berthier, E., Vadon, H., Baratoux, D., Arnaud, Y., Vincent, C., Feigl, K., Rémy, F., Legrésy, B., 2005. Surface motion of mountain glaciers derived from satellite optical imagery. Remote Sens. Environ. 95 (1), 14–28 Mar.

Binet, R., Bollinger, L., 2005. Horizontal coseismic deformation of the 2003 Bam (Iran) earthquake measured from SPOT-5 THR satellite imagery. Geophys. Res. Lett. 32 (2), L02307.

Bulmer, M.H., Johnston, A., Engle, F., Salas, 1999. Seismically triggered slope failures in the Colca Valley, Southern Peru. In: EOS Trans. vol. H41A-07. pp. S127.

Casson, B., Delacourt, C., Baratoux, D., Allemand, P., 2003. Seventeen years of the "la Clapière" landslide evolution analysed from ortho-rectified aerial photographs. Eng. Geol. 68 (1), 123–139.

Casu, F., Manconi, A., Pepe, A., Lanari, R., 2011. Deformation time-series generation in areas characterized by large displacement dynamics: the SAR amplitude pixel-offset SBAS technique. IEEE Trans. Geosci. Remote Sens. 49 (7), 2752–2763.

Cavalié, O., Doin, M.-P., Lasserre, C., Briole, P., 2007. Ground motion measurement in the Lake Mead area, Nevada, by differential synthetic aperture radar interferometry time series analysis: probing the lithosphere rheological structure. J. Geophys. Res. Solid Earth 112 (B3), B03403.

Chau, K.T., 1995. Landslides modeled as bifurcations of creeping slopes with nonlinear friction law. Int. J. Solids Struct. 32 (23), 3451–3464.

Chlieh, M., Perfettini, H., Tavera, H., Avouac, J.-P., Remy, D., Nocquet, J.-M., Rolandone, F., Bondoux, F., Gabalda, G., Bonvalot, S., 2011. Interseismic coupling and seismic potential along the Central Andes subduction zone. J. Geophys. Res. 116 (B12), B12405.

Dadson, S.J., Hovius, N., Chen, H., Dade, W.B., Lin, J.-C., Hsu, M.-L., Lin, C.-W., Horng, M.-J., Chen, T.-C., Milliman, J., Stark, C.P., 2004. Earthquake-triggered increase in sediment delivery from an active mountain belt. Geology 32 (8), 733–736.

Dehecq, A., Gourmelen, N., Trouve, E., 2015. Deriving large-scale glacier velocities from a complete satellite archive: application to the Pamir-Karakoram-Himalaya. Remote Sens. 162, 55–66.

Delacourt, C., Allemand, P., Casson, B., Vadon, H., 2004. Velocity field of the La Clapière landslide measured by the correlation of aerial and QuickBird satellite images. Geophys. Res. Lett. 31 (15).

Doin, M.-P., Lodge, F., Guillaso, S., Jolivet, R., Lasserre, C., Ducret, G., Grandin, R., Pathier, E., Pinel, V., 2011. Presentation of the small baseline NSBAS processing chain on a case example: the Etna deformation monitoring from 2003 to 2010 using Envisat data. In: FRINGE 2011 ESA Conference.

Efron, B., Gong, G., 1983. A leisurely look at the bootstrap, the jackknife, and cross-validation. Am. Stat. 37 (1), 36–48.

Eilertsen, R.S., Hansen, L., Bargel, T.H., Solberg, I.-L., 2008. Clay slides in the Målselv Valley, northern Norway: characteristics, occurrence, and triggering mechanisms. Geomorphology 93 (3), 548–562.

Fahnestock, M., Scambos, T., Moon, T., Gardner, A., Haran, T., Klinger, M., 2015. Rapid large-area mapping of ice flow using Landsat 8. Remote Sens. Environ.

Handwerger, A.L., Rempel, A.W., Skarbek, R.M., Roering, J.J., Hilley, G.E., 2016. Rate-weakening friction characterizes both slow sliding and catastrophic failure of landslides. Proc. Natl. Acad. Sci. 113 (37), 10281–10286.

Handwerger, A.L., Roering, J.J., Schmidt, D.A., 2013. Controls on the seasonal deformation of slow-moving landslides. Earth Planet. Sci. Lett. 377-378, 239–247.

Heid, T., Kääb, A., 2012. Repeat optical satellite images reveal widespread and long term decrease in land-terminating glacier speeds. Cryosphere 6 (2), 467–478.

Helmstetter, A., Sornette, D., Grasso, J.-R., Andersen, J.V., Gluzman, S., Pisarenko, V., 2004. Slider block friction model for landslides: application to Vaiont and La Clapière landslides. J. Geophys. Res. 109, 15.

Hungr, O., Leroueil, S., Picarelli, L., 2014. The Varnes classification of landslide types, an update. Landslides 11 (2), 167–194.

Iverson, R.M., 2000. Landslide triggering by rain infiltration. Water Resour. Res. 36 (7), 1897.

Jibson, R.W., Prentice, C.S., Borissoff, B.A., Rogozhin, E.A., Langer, C.J., 1994. Some observations of landslides triggered by the 29 April 1991 Racha earthquake, Republic of Georgia. Bull. Seismol. Soc. Am. 84 (4), 963–973.

Jongmans, D., Bièvre, G., Schwartz, S., Renalier, F., Beaurez, N., 2009. Geophysical investigation of the large Avignonet landslide in glaciolacustrine clays in the Trièves

area (French Alps). Eng. Geol. 109, 45–56.

Kääb, A., 2002. Monitoring high-mountain terrain deformation from repeated air- and spaceborne optical data: examples using digital aerial imagery and ASTER data. ISPRS J. Photogramm. Remote Sens. 57 (1-2), 39–52.

Lacroix, P., Berthier, E., Maquerhua, E.T., 2015. Earthquake-driven acceleration of slow-moving landslides in the Colca Valley, Peru, detected from Pléiades images. Remote Sens. Environ. 165, 148–158.

Lacroix, P., Perfettini, H., Taipe, E., Guillier, B., 2014. Co- and postseismic motion of a landslide; observations, modelling and analogy with tectonic faults. Geophys. Res. Lett.

Leprince, S., Barbot, S., Ayoub, F., Avouac, J.-P., 2007. Automatic and precise orthor-ectification, coregistration, and subpixel correlation of satellite images, application to ground deformation measurements. IEEE Trans. Geosci. Remote Sens. 45 (6), 1529–1558. http://dx.doi.org/10.1109/TGRS.2006.888937.

Leprince, S., Muse, P., Avouac, J.P., 2008. In-flight CCD distortion calibration for pushbroom satellites based on subpixel correlation. IEEE Trans. Geosci. Remote Sens. 46 (9), 2675–2683.

Lin, G.-W., Chen, H., Chen, Y.-H., Horng, M.-J., 2008. Influence of typhoons and earthquakes on rainfall-induced landslides and suspended sediments discharge. Eng. Geol. 97 (1-2), 32–41.

López-Quiroz, P., Doin, M.-P., Tupin, F., Briole, P., Nicolas, J.-M., 2009. Time series analysis of Mexico City subsidence constrained by radar interferometry. J. Appl. Geophys. 69 (1), 1–15.

Mansour, M.F., Morgenstern, N.R., Martin, C.D., 2011. Expected damage from displacement of slow-moving slides. Landslides 8 (1), 117–131.

Marc, O., Hovius, N., Meunier, P., Uchida, T., Hayashi, S.-I., 2015. Transient changes of landslide rates after earthquakes. Geology.

Michel, R., Avouac, J.-P., 2002. Deformation due to the 17 August 1999 Izmit, Turkey, earthquake measured from SPOT images. J. Geophys. Res. Solid Earth 107 (B4) ETG 2–1.

Moro, M., Chini, M., Saroli, M., Atzori, S., Stramondo, S., Salvi, S., 2011. Analysis of large, seismically induced, gravitational deformations imaged by high-resolution COSMO-SkyMed synthetic aperture radar. Geology 39 (6), 527–530.

Petley, D., Bulmer, M.H., Murphy, W., 2002. Patterns of movement in rotational and translational landslides. Geology 30 (8), 719–722.

Scherler, D., Leprince, S., Strecker, M.R., 2008. Glacier-surface velocities in alpine terrain

from optical satellite imagery accuracy improvement and quality assessment. Remote Sens. Environ. 112 (10), 3806–3819.

Schulz, W.H., Kean, J.W., Wang, G., 2009. Landslide movement in southwest Colorado triggered by atmospheric tides. Nat. Geosci. 2 (12), 863–866.

Strozzi, T., Delaloye, R., Kääb, A., Ambrosi, C., Perruchoud, E., Wegmuller, U., 2010. Combined observations of rock mass movements using satellite SAR interferometry, differential GPS, airborne digital photogrammetry, and airborne photography interpretation. J. Geophys. Res. 115, 11.

Stumpf, A., Malet, J.P., Allemand, P., Ulrich, P., 2014. Surface reconstruction and landslide displacement measurements with Pléiades satellite images. ISPRS J. Photogramm. Remote Sens. 95, 1–12.

Stumpf, A., Malet, J.-P., Delacourt, C., 2017. Correlation of satellite image time-series for the detection and monitoring of slow-moving landslides. Remote Sens. Environ. 189 (Supplement C), 40–55.

Stumpf, A., Malet, J.-P., Puissant, A., Travelletti, J., 2016. Monitoring of Earth Surface Motion and Geomorphologic Processes by Optical Image Correlation. In: pp. 147–190.

Taylor, M.H., Leprince, S., Avouac, J.-P., Sieh, K., 2008. Detecting co-seismic displacements in glaciated regions: an example from the great November 2002 Denali earthquake using SPOT horizontal offsets. Earth Planet. Sci. Lett. 270 (3-4), 209–220.

Thouret, J.-C., Wörner, G., Gunnell, Y., Singer, B., Zhang, X., Souriot, T., 2007. Geochronologic and stratigraphic constraints on canyon incision and Miocene uplift of the Central Andes in Peru. Earth Planet. Sci. Lett. 263 (3-4), 151–166.

Travelletti, J., Delacourt, C., Allemand, P., Malet, J.P., Schmittbuhl, J., Toussaint, R., Bastard, M., 2012. Correlation of multi-temporal ground-based optical images for landslide monitoring: application, potential and limitations. ISPRS J. Photogramm. Remote Sens. 70 (Supplement C), 39–55.

Van Asch, T.W.J., Buma, J., Van Beek, L.P.H., 1999. A view on some hydrological triggering systems in landslides. Geomorphology 30 (1), 25–32.

Van Puymbroeck, N., Michel, R., Binet, R., Avouac, J.-P., Taboury, J., 2000. Measuring earthquakes from optical satellite images. Appl. Opt. 39 (20), 3486–3494 Jul.

Zerathe, S., Lacroix, P., Jongmans, D., Marino, J., Taipe, E., Wathelet, M., Pari, W., Smoll, L.F., Norabuena, E., Guillier, B., Tatard, L., 2016. Morphology, structure and kinematics of a rainfall controlled slow-moving Andean landslide, Peru: the Maca slow-moving Andean landslide. Earth Surf. Process. Landf. 41 (11), 1477–1493.